

Online Graph Learning via Time-Vertex Adaptive Filters: From Theory to Cardiac Fibrillation

Alexander Jenkins^{*,1,2}, Thiernithi Varidhisai^{*,1}, Ahmed El-Medany²,
Fu Siong Ng² and Danilo Mandic¹, *Fellow, IEEE*

Abstract—Graph Signal Processing (GSP) provides a powerful framework for analysing complex, interconnected systems by modelling data as signals on graphs. Recent advances in GSP have enabled the learning of graph structures from observed signals, but these methods often struggle with time-varying systems and real-time applications. Adaptive filtering techniques, while effective for online learning, have seen limited application in graph topology estimation from a GSP perspective. To this end, we introduce AdaCGP, an online algorithm for adaptive estimation of the Graph Shift Operator (GSO) from multivariate time series. The GSO is estimated from an adaptive time-vertex autoregressive model through recursive update formulae designed to address sparsity, shift-invariance and bias. Through simulations, we show that AdaCGP performs consistently well across various graph topologies, and achieves improvements in excess of 82% for GSO estimation compared to baseline adaptive vector autoregressive models. In addition, our online variable splitting approach for enforcing sparsity enables near-perfect precision in identifying causal connections while maintaining low false positive rates upon optimisation of the forecast error. Finally, AdaCGP’s ability to track changes in graph structure is demonstrated on recordings of ventricular fibrillation dynamics in response to an anti-arrhythmic drug. AdaCGP is shown to be able to identify the stability of critical conduction patterns that may be maintaining the arrhythmia in an intuitive way, together with its potential to support diagnosis and treatment strategies.

Index Terms—Graph topology learning, adaptive graph signal processing, graph shift operator, time-vertex stochastic process, multivariate statistical models, cardiac fibrillation.

I. INTRODUCTION

IN an era of unprecedented data generation, the challenge of understanding complex, time-varying systems has become increasingly critical. Much of this data arrives as simultaneous, long-running time series from diverse sources including financial markets, environmental monitoring stations [2], energy grid networks [3], and biomedical sensors [4]. While often appearing unstructured, these datasets frequently encode underlying spatiotemporal relationships that can reveal the underlying system dynamics.

This is particularly evident in complex cardiac arrhythmias, such as Ventricular Fibrillation (VF) and Atrial Fibrillation (AF), where chaotic electrical propagation manifests

as patient-specific ‘electrophenotypes’ [5], [6]. The ability to capture the electrophenotype and assess its stability holds crucial diagnostic value, yet current treatments remain rife due to our inability to characterise these patterns, leading to poor outcomes and high recurrence rates [5], [7]. The development of adaptive, data-driven approaches to address this challenge is therefore essential, both for advancing cardiac fibrillation treatment and for analysing other complex systems.

Networks/graphs provide a powerful low-dimensional framework for representing relationships between data sources [8], with nodes representing sensors and edges capturing their dependencies. When the graph structure is known, various tools from GSP theory and machine learning can analyse signals residing on the graph [9], [10]. However, in many real-world scenarios, the underlying graph structure is unknown and must be inferred from observed data. The GSO, which can take forms such as the adjacency matrix or Laplacian matrix, represents this structure by encoding the relationships between nodes. While existing approaches based on sparse inverse covariance estimation [11], signal smoothness [12], [13], and signal diffusion [14]–[16] have shown promise in learning GSOs, they typically focus on learning variants of the Laplacian or symmetric matrices, and neglect temporal dependencies. Also, many applications require learning more general forms of the GSO, such as the directed weighted adjacency matrix, that can capture asymmetric relationships and potential causal connections between nodes.

In the context of time series data, vector autoregressive (VAR) models are commonly used to uncover a causal graph representation between the variables, as popularised by Granger [17]. More recently, GSP methods have been proposed to learn graph structures from multivariate time series. For instance, Segarra *et al.* [18] investigated the joint identification of graph filters and input signals, and Mei and Moura [19] proposed estimating GSOs through an autoregressive time-vertex system identification problem. However, these methods typically operate in a batch processing mode, which becomes inefficient and impractical when dealing with streaming data from complex systems where the graph structure is often time-varying [20]. In such cases, batch processing would require rerunning the model each time new data arrives, leading to high computational costs.

Adaptive signal processing techniques are well-suited for such online learning scenarios. Algorithms like the Least Mean Square (LMS) [21], Recursive Least Squares (RLS) [22], and RLS-like LMS variants [23] provide powerful tools for learning and tracking time-varying parameters. Recent works

* These authors contributed equally.

¹ Department of Electrical and Electronic Engineering, Imperial College London, London, SW7 2AZ, United Kingdom.

² National Heart and Lung Institute, Imperial College London, London, United Kingdom.

Correspondence to: Alexander Jenkins <a.jenkins21@imperial.ac.uk>.

An earlier version of the core algorithm was presented in preprint form [1]. The current manuscript represents a comprehensive advancement with extended theoretical analysis, synthetic experiments, and a real-world case study on cardiac fibrillation.

have introduced online schemes for estimating causal graphs from sparse VAR processes, such as TISO (Topology Identification via Sparse Online learning) and its RLS counterpart TIRSO [24]. While adaptive filtering techniques have been extended to GSP [25]–[27], current research has focused on signal estimation and sampling on graphs. The problem of adaptive graph learning from streaming data remains largely unexplored.

To address this gap, we leverage time-vertex GSP theory to learn and track changes in weighted graph adjacency matrices. Our main contributions are:

- 1) An online time-vertex adaptive filtering algorithm, termed *AdaCGP*, that extends Mei and Moura’s [19] offline approach for graph structure learning;
- 2) A variable splitting approach for achieving true sparsity in online GSO estimation, enabling reliable identification of non-zero causal elements and efficient computation through sparse matrix operations;
- 3) A rigorous empirical analysis on synthetic data demonstrating the convergence and superiority of *AdaCGP* over adaptive VAR models, with prediction (forecast) error optimisation enabling reliable hyperparameter selection and GSO sparsity estimation;
- 4) An application to VF recordings across increasing anti-arrhythmic drug concentrations to regulate electrophenotypic complexity, demonstrating the ability of *AdaCGP* to capture the structure and stability of cardiac fibrillation.

The remainder of this paper is structured as follows. Section II provides background on graph and time-vertex signal processing, followed by the formulation of our optimisation objectives in Section III and presentation of our adaptive algorithm in Section IV. We then validate our approach on synthetic data in Section V before demonstrating its application to real-world cardiac fibrillation data in Section VI. Finally, Section VII presents our conclusions.

II. BACKGROUND

This section introduces the fundamental concepts of GSP and presents the Causal Graph Process (CGP) model for capturing temporal and structural dependencies in time-varying random graph signals.

A. Graph Structure and Signals

A graph $\mathcal{G} = (\mathcal{V}, \mathcal{E})$ is a mathematical structure that captures the relationships between a set of entities. It consists of a set of N nodes, $\mathcal{V} = \{v_1, \dots, v_N\}$, and a set of edges, \mathcal{E} , representing their connections. A weight matrix, $\mathbf{W} \in \mathbb{R}^{N \times N}$, encodes the strength and pattern of the edge connections. This matrix, commonly referred to as the GSO in GSP, has entries w_{ij} that are nonzero only if there is an edge connecting nodes i and j , i.e., $(i, j) \in \mathcal{E}$. On this structure, a graph signal is defined as a function $f : \mathcal{V} \rightarrow \mathbb{R}$ that assigns a real value to each node, represented as a vector $\mathbf{x} = [x_1, \dots, x_N]^T \in \mathbb{R}^{N \times 1}$, where x_n is the signal value at node v_n .

B. Graph Filtering

Graph filtering is a fundamental operation in GSP that extends classical filtering to the graph domain. A graph filter is commonly expressed as a polynomial of the GSO, that is

$$H_L(\mathbf{W}, \mathbf{h}) = \sum_{l=0}^L h_l \mathbf{W}^l = h_0 \mathbf{I} + h_1 \mathbf{W} + \dots + h_L \mathbf{W}^L, \quad (1)$$

where $\mathbf{h} = [h_0, \dots, h_L]^T$ is a vector of filter coefficients and filter order L determines the neighbourhood size over which it operates.

Polynomial graph filters are shift-invariant, meaning that filtering a shifted graph signal is equivalent to shifting the filtered signal, i.e., $H_L(\mathbf{W}, \mathbf{h})(\mathbf{W}\mathbf{x}) = \mathbf{W}(H_L(\mathbf{W}, \mathbf{h})\mathbf{x})$. This shift-invariant property has two important implications. First, that the graph filter commutes with the GSO,

$$[H_L(\mathbf{W}, \mathbf{h}), \mathbf{W}] = \mathbf{0}, \quad (2)$$

and second, that graph filters commute with each other

$$[H_L(\mathbf{W}, \mathbf{h}_1), H_K(\mathbf{W}, \mathbf{h}_2)] = \mathbf{0}. \quad (3)$$

Here, the commutator notation $[\cdot, \cdot]$ for two operators \mathcal{A} and \mathcal{B} is defined as

$$[\mathcal{A}, \mathcal{B}] \triangleq \mathcal{A}\mathcal{B} - \mathcal{B}\mathcal{A}, \quad (4)$$

where $[\mathcal{A}, \mathcal{B}] = 0$ indicates that the operators commute [9].

C. Causal Graph Process

The CGP is a time-vertex model for random time-varying graph signals [19]. It is a special case of the more general VAR moving average time-vertex model [28], which expresses the VAR coefficients as shift-invariant graph filters. The CGP model is given by

$$\mathbf{x}_t = \sum_{p=1}^P H_p(\mathbf{W}, \mathbf{h}_p) \mathbf{x}_{t-p} + \mathbf{w}_t, \quad (5)$$

where \mathbf{x}_t is the graph signal at time step t , $H_p(\mathbf{W}, \mathbf{h}_p)$ is an order p graph filter as defined in (1), and $\mathbf{w}_t \sim \mathcal{N}(\mathbf{0}, \mathbf{I}_N)$.

The CGP model is causal in the sense that the signal at a node at time t can only be influenced by its P -hop neighbourhood from the previous P time steps. Mathematically, this is reflected in the order of the polynomial coefficients being bounded by the lag p , $p = 1, \dots, P$.

This structure models information propagation through the graph at a fixed speed (one graph shift per sampling period). While more general formulations that decouple the polynomial order from the time lag are more expressive [28], the CGP model’s coupled temporal and spatial dependencies provide a tractable framework for graph learning [19]. The sampling frequency of discrete-time models can also be chosen to align with the propagation speed, making this assumption rather reasonable in practice.

Remark 1. *The CGP model is inherently weakly stationary due to its formulation as a sum of shift-invariant graph filters (as defined in [29]). While stationarity assumptions enable the definition of meaningful optimality criteria for filter design, real-world scenarios often involve non-stationary signals*

and time-varying graph structures. This motivates adaptive approaches that can track gradual changes through recursive optimisation of these criteria.

III. OBJECTIVES FOR ONLINE OPTIMISATION

Having established the CGP model structure, we now address the problem of parameter estimation. The CGP model in (5) can be formulated as a multivariate linear regression problem for estimating \mathbf{W} and \mathbf{h}_p for $p = 1, \dots, P$, where the Mean Square Error (MSE) is the optimal linear estimator [30]. In this work, we adopt the least squares method, a deterministic counterpart of the MSE estimator [21]. Specifically, we employ the RLS-like LMS scheme [23] for recursive optimisation. This approach incorporates a forgetting factor λ into the LMS objective and has been shown to achieve fast convergence and tracking performance similar to RLS while being more numerically stable, as it does not involve matrix inversion. The least squares problem of (5) is formulated as

$$\min_{\mathbf{W}, \mathbf{h}} \frac{1}{2} \sum_{\tau=1}^t \lambda^{t-\tau} \left\| \mathbf{x}_\tau - \sum_{p=1}^P H_p(\mathbf{W}, \mathbf{h}_p) \mathbf{x}_{\tau-p} \right\|_2^2, \quad (6)$$

where $\mathbf{h} = [\mathbf{h}_1^T, \dots, \mathbf{h}_P^T]^T \in \mathbb{R}^{M \times 1}$ with $M = P(P+3)/2$, $\mathbf{x}_\tau = \mathbf{0}$ for $\tau \leq 0$, and $\lambda \in (0, 1]$. It is important to note that (6) represents a non-convex optimisation problem due to the polynomial in \mathbf{W} . To address this, we follow the approach proposed by Mei and Moura [19] and cast the problem into alternating steps of convex regularised least squares sub-problems.

A. Solving for $\Psi_p = H_p(\mathbf{W}, \mathbf{h}_p)$

The optimisation objective is first reformulated to solve for $\Psi_p = H_p(\mathbf{W}, \mathbf{h}_p)$ instead of \mathbf{W} and \mathbf{h} directly, where we denote our estimate as $\hat{\Psi}_p$. This transformation makes the problem quadratic in Ψ_p . Upon incorporating sparsity regularisation, we arrive at the following optimisation problem

$$\min_{\Psi} \frac{1}{2} \sum_{\tau=1}^t \lambda^{t-\tau} \left\| \mathbf{x}_\tau - \sum_{p=1}^P \Psi_p \mathbf{x}_{\tau-p} \right\|_2^2 + \sum_{p=1}^P \mu_p \|\text{vec}(\Psi_p)\|_1, \quad (7)$$

where $\Psi = [\Psi_1, \dots, \Psi_P] \in \mathbb{R}^{N \times NP}$ is a concatenation of the P graph filters, $\text{vec}(\cdot)$ is a vectorisation operator that stacks the columns of the matrix it acts on, and $\|\cdot\|_1$ is an ℓ_1 norm, while μ_p is a constant which adjusts the degree of sparsity of the corresponding Ψ_p .

To enforce that graph filters are shift-invariant, a soft constraint is added

$$\min_{\Psi} \frac{1}{2} \sum_{\tau=1}^t \lambda^{t-\tau} \left\| \mathbf{x}_\tau - \sum_{p=1}^P \Psi_p \mathbf{x}_{\tau-p} \right\|_2^2 + \sum_{p=1}^P \mu_p \|\text{vec}(\Psi_p)\|_1 + \gamma \sum_{i \neq j} \|\Psi_i - \Psi_j\|_F^2, \quad (8)$$

where the additional term, weighted by γ , enforces the graph filters to commute as defined in (3). This formulation results in a quartic programming problem. However, as noted in [19], the objective is multi-convex and naturally leads to block coordinate descent as a solution, despite not being optimal in MSE. In other words, when all Ψ_j except for Ψ_i are held constant, the problem becomes a convex optimisation in Ψ_i .

B. Estimating \mathbf{W} from $\hat{\Psi}_1$

From the definition of the graph filter in (1), Ψ_1 is a linear function of \mathbf{W} . Its estimate, $\hat{\Psi}_1$, therefore provides a reasonable (yet biased) approximation of \mathbf{W} . However, to determine the true \mathbf{W} after obtaining $\hat{\Psi}$ from (7) or (8), the following regularised least squares sub-problem is used

$$\min_{\mathbf{W}} \frac{1}{2} \left\| \hat{\Psi}_1 - \mathbf{W} \right\|_2^2 + \mu_1 \|\text{vec}(\mathbf{W})\|_1 + \gamma \sum_{p=2}^2 \|\mathbf{W}, \hat{\Psi}_p\|_F^2. \quad (9)$$

where the final term enforces the shift-invariant property in (2) by ensuring that $\hat{\mathbf{W}}$ commutes with all $\hat{\Psi}_p$.

When (8) is used to calculate $\hat{\Psi}_1$, the optimisation sub-problem in (9) may be bypassed by the approximation $\hat{\mathbf{W}} = \hat{\Psi}_1$, since the shift invariance property has already been enforced. We denote this latter variant of our algorithm as **Path 2**, which is detailed further in subsequent sections.

C. Estimating \mathbf{h}

Upon estimating $\hat{\mathbf{W}}$, we can re-frame the initial objective in (6) as a quadratic optimisation with respect to \mathbf{h} . Assuming sparsity in \mathbf{h} , we can substitute (1) into (6) and rearrange to give

$$\min_{\mathbf{h}} \frac{1}{2} \sum_{\tau=1}^t \lambda^{t-\tau} \|\mathbf{x}_\tau - \mathbf{Y}_\tau \mathbf{h}\|_2^2 + \eta \|\mathbf{h}\|_1, \quad (10)$$

where η controls for the degree of sparsity and

$$\mathbf{Y}_t = [\mathbf{x}_{t-1}, \hat{\mathbf{W}} \mathbf{x}_{t-1}, \dots, \mathbf{x}_{t-P}, \dots, \hat{\mathbf{W}}^P \mathbf{x}_{t-P}]. \quad (11)$$

The dimensions of \mathbf{Y}_t are $N \times M$, where $M = P(P+3)/2$. Despite the apparent size of M , practical applications often involve a much lower order, frequently satisfying $M < N$. It is important to note that this step, while informative, is not critical to our primary goal of recovering \mathbf{W} .

IV. ONLINE ESTIMATION ALGORITHM

We introduce AdaCGP (Adaptive identification of Causal Graph Processes), an algorithm designed to achieve sparse online solutions to the objective in (6). While existing online methods such as ℓ_1 -regularised LMS [31] and oracle algorithms [32] achieve low MSE, they rarely produce truly sparse solutions compared to offline methods like basis pursuit [33]. This is an important limitation in our context for estimating $\hat{\mathbf{W}}$, since sparsity directly determines the presence or absence of edges in the graph structure, driving a causal interpretation.

To overcome this issue, we adapt the offline variable splitting approach of Schmidt *et al.* [34] to the online objective in (6), reformulating the alternating ℓ_1 -regularised sub-problems in (8) and (9) by splitting the target variables ($\hat{\Psi}$ and $\hat{\mathbf{W}}$) into their positive and negative components as

$$\hat{\Psi} \triangleq \hat{\Psi}_+ - \hat{\Psi}_-, \quad (12)$$

$$\hat{\mathbf{W}} \triangleq \hat{\mathbf{W}}_+ - \hat{\mathbf{W}}_-, \quad (13)$$

where $(\cdot)_+ \geq \mathbf{0}$ and $(\cdot)_- \geq \mathbf{0}$ contain only the positive and negative parts of (\cdot) , respectively. The ℓ_1 -norm can then be expressed as a product-weighted sum. For the matrices $\hat{\Psi}$ and $\hat{\mathbf{W}}$, this is given by

$$\|\hat{\Psi}\|_1 = \text{Tr}(\mathbf{1}_{N \times N} \hat{\Psi}_+) + \text{Tr}(\mathbf{1}_{N \times N} \hat{\Psi}_-),$$

$$\|\hat{\mathbf{W}}\|_1 = \text{Tr}(\mathbf{1}_{N \times N} \hat{\mathbf{W}}_+) + \text{Tr}(\mathbf{1}_{N \times N} \hat{\mathbf{W}}_-)$$

where $\text{Tr}(\cdot)$ is the trace operator and $\mathbf{1}_{N \times N} \in \mathbb{R}^{N \times N}$ is a matrix of unities.

These reformulations convert our first two sub-problems into non-negativity constrained optimisations [34], which we solve via projected stochastic gradient descent using the recursive update formulae we derive next.

Remark 2. *The variable splitting approach in (12) and (13) offers potential for incorporating prior knowledge about the GSO structure. For example, when the GSO represents an adjacency matrix (elements in $\{0, 1\}$), setting $\hat{\Psi}_- = \hat{\mathbf{W}}_- = \mathbf{0}$ naturally enforces this constraint as an inductive bias. While Laplacian matrices could be split into their positive diagonal and negative off-diagonal elements, their zero row sum proves challenging to maintain iteratively without resorting to Lagrangian methods. To maintain generality across different GSO structures, we follow the approach in [19] and study the unconstrained case.*

A. Updating Ψ_t

To minimise (8) at time instant t , we calculate its gradient with respect to the positive part of each p^{th} block of the graph filter $\hat{\Psi}_p$, i.e. $(\hat{\Psi}_p)_+$, which is given by

$$\begin{aligned} \nabla_{(\hat{\Psi}_p)_+}^{(t)} &= \sum_{\tau=1}^t \lambda^{t-\tau} \left(\sum_{k=1}^P \hat{\Psi}_{k,t-1} \mathbf{x}_{\tau-k} \mathbf{x}_{\tau-p}^T - \mathbf{x}_{\tau} \mathbf{x}_{\tau-p}^T \right) \\ &+ \mu_{p,t} \mathbf{1}_{N \times N} + \gamma \mathbf{Q}_{p,t}, \end{aligned} \quad (14)$$

where the gradient of the commutative term is given by

$$\mathbf{Q}_{p,t+1} = \sum_{k \neq p}^P \left(\left[\hat{\Psi}_{p,t}, \hat{\Psi}_{k,t} \right] \hat{\Psi}_{k,t}^T - \hat{\Psi}_{k,t}^T \left[\hat{\Psi}_{p,t}, \hat{\Psi}_{k,t} \right] \right), \quad (15)$$

where we use $(\cdot)_t$ to denote variables (\cdot) at the time instant t . We define $\hat{\Psi}_t$, \mathbf{M}_t , and \mathbf{Q}_t as the concatenation of graph filters, sparsity and commutative terms over all P , given by

$$\hat{\Psi}_t \triangleq \left[\hat{\Psi}_{1,t}, \hat{\Psi}_{2,t}, \dots, \hat{\Psi}_{P,t} \right] := \hat{\Psi}_{+t} - \hat{\Psi}_{-t},$$

$$\mathbf{M}_t \triangleq [\mu_{1,t} \mathbf{1}_{N \times N}, \mu_{2,t} \mathbf{1}_{N \times N}, \dots, \mu_{P,t} \mathbf{1}_{N \times N}],$$

and

$$\mathbf{Q}_t \triangleq [\mathbf{Q}_{1,t}, \mathbf{Q}_{2,t}, \dots, \mathbf{Q}_{P,t}],$$

where $\hat{\Psi}_t$ is expressed as the difference between its positive and negative parts, as in (12), and $\hat{\Psi}_t$, \mathbf{M}_t and \mathbf{Q}_t are matrices in $\mathbb{R}^{N \times NP}$.

Next, we use $\mathbf{R}_t \in \mathbb{R}^{NP \times NP}$ to denote the accumulated correlation matrix of the lagged input signals, and $\mathbf{P}_t \in \mathbb{R}^{N \times NP}$ to denote the accumulated cross-correlation matrix between the input signals $\mathbf{x}_{P,t}$ and the desired responses \mathbf{x}_t , where

$$\mathbf{x}_{P,t} \triangleq [\mathbf{x}_{t-1}^T, \mathbf{x}_{t-2}^T, \dots, \mathbf{x}_{t-P}^T]^T \in \mathbb{R}^{NP \times 1}.$$

We can now write the recursive update formulae to \mathbf{R}_t and \mathbf{P}_t as

$$\mathbf{R}_t \triangleq \sum_{\tau=1}^t \lambda^{t-\tau} \mathbf{x}_{P,\tau} \mathbf{x}_{P,\tau}^T = \lambda \mathbf{R}_{t-1} + \mathbf{x}_{P,t} \mathbf{x}_{P,t}^T,$$

and

$$\mathbf{P}_t \triangleq \sum_{\tau=1}^t \lambda^{t-\tau} \mathbf{x}_{\tau} \mathbf{x}_{P,\tau}^T = \lambda \mathbf{P}_{t-1} + \mathbf{x}_t \mathbf{x}_{P,t}^T.$$

These expressions are then substituted into (14) to give

$$\mathbf{G}_t \triangleq \left[\nabla_{(\hat{\Psi}_1)_+}^{(t)}, \dots, \nabla_{(\hat{\Psi}_P)_+}^{(t)} \right] \triangleq \hat{\Psi}_{t-1} \mathbf{R}_t - (\mathbf{P}_t - \gamma \mathbf{Q}_t), \quad (16)$$

where it can be shown straightforwardly that $\nabla_{(\hat{\Psi}_p)_+}^{(t)} = \nabla_{(\hat{\Psi}_p)_+}^{(t)}$ and $\nabla_{(\hat{\Psi}_p)_-}^{(t)} = -\nabla_{(\hat{\Psi}_p)_-}^{(t)}$ for all p .

Finally, we can now express the updates to our first sub-problem as a gradient projection, that is

$$\hat{\Psi}_{+t} = \left(\hat{\Psi}_{+t-1} - (\mathbf{M}_t + \mathbf{G}_t)(\mathbf{A}_t \otimes \mathbf{I}_{N \times N}) \right)_+,$$

where $\mathbf{A}_t = \text{diag}(\alpha_1, \alpha_2, \dots, \alpha_P) \in \mathbb{R}^{P \times P}$ is a diagonal matrix of stepsizes for each filter block. Similarly, the update equation for $\hat{\Psi}_{-t}$ can be obtained as

$$\hat{\Psi}_{-t} = \left(\hat{\Psi}_{-t-1} - (\mathbf{M}_t - \mathbf{G}_t)(\mathbf{A}_t \otimes \mathbf{I}_{N \times N}) \right)_+.$$

Then, finally $\hat{\Psi}_t = \hat{\Psi}_{+t} - \hat{\Psi}_{-t}$ can be set.

Having derived the update equations for $\hat{\Psi}_t$, we next analyse the computational complexity per iteration. The cost is dominated by the gradient calculation in (16). Computing $\hat{\Psi}_{t-1} \mathbf{R}_t$ and \mathbf{Q}_t requires $\mathcal{O}(N^3 P^2)$ operations in the dense case. Since our algorithm explicitly zeros out elements of $\hat{\Psi}_t$, sparse matrix operations could be used. With $S_t = \|\hat{\Psi}_t\|_0$ total non-zeros and $S_{p,t} = \max_p \|\hat{\Psi}_{p,t}\|_0$ maximum non-zeros per block at time t , the complexity reduces to $\mathcal{O}(S_{t-1} NP)$ for $\hat{\Psi}_{t-1} \mathbf{R}_t$ and $\mathcal{O}(S_{p,t-1}^2 P)$ for \mathbf{Q}_t . Since $S_{t-1} \leq N^2 P$, $S_{p,t-1} \leq N^2$, and $S_{t-1} \geq S_{p,t-1}$, the total complexity simplifies to $\mathcal{O}(S_{t-1} NP)$, which scales more favourably for large data applications.

B. Updating \mathbf{W}_t

The next step of our algorithm involves recovering the GSO, $\hat{\mathbf{W}}_t$, from $\hat{\Psi}_t$ through either of two paths. **Path 2** provides a simple but biased estimate by setting $\hat{\mathbf{W}}_t = \hat{\Psi}_{1,t}$. **Path**

1, which we detail below, optimises (9) to obtain unbiased estimates of $\hat{\mathbf{W}}_t$ at the expense of computational complexity.

In Path 1, we simplify (16) in the first sub-problem by setting $\mathbf{Q}_t = \mathbf{0}$ for all time steps t . This makes the first sub-problem convex by deferring the enforcement of shift-invariance to this phase instead. To optimise (9), the variable splitting approach from (13) is followed to express $\hat{\mathbf{W}}_t$ as the difference between its positive and negative parts. Computing the gradient of (9) with respect to the positive elements of $\hat{\mathbf{W}}_t$ gives

$$\mathbf{V}_t = \hat{\mathbf{W}}_{t-1} - (\hat{\Psi}_{1,t} - \gamma \mathbf{S}_t), \quad (17)$$

where the gradient of the commutative term is given by

$$\mathbf{S}_t = \sum_{k=2}^P \left(\left[\hat{\mathbf{W}}_{t-1}, \hat{\Psi}_{k,t} \right] \hat{\Psi}_{k,t}^T - \hat{\Psi}_{k,t}^T \left[\hat{\mathbf{W}}_{t-1}, \hat{\Psi}_{k,t} \right] \right). \quad (18)$$

The parameter updates can again be expressed as gradient projections

$$\hat{\mathbf{W}}_{+t} = \left(\hat{\mathbf{W}}_{+t-1} - \beta_t (\mu_{1,t} \mathbf{1}_{N \times N} + \mathbf{V}_t) \right)_+,$$

and

$$\hat{\mathbf{W}}_{-t} = \left(\hat{\mathbf{W}}_{-t-1} - \beta_t (\mu_{1,t} \mathbf{1}_{N \times N} - \mathbf{V}_t) \right)_+,$$

where β_t is the stepsize, and $\mu_{1,t}$ is the sparsity parameter from the first sub-problem. Then, $\hat{\mathbf{W}}_t = \hat{\mathbf{W}}_{+t} - \hat{\mathbf{W}}_{-t}$.

The computational complexity for updating $\hat{\mathbf{W}}_t$ varies between paths. While Path 2 requires $\mathcal{O}(N^2)$ operations for direct assignment of $\hat{\mathbf{W}}_t = \hat{\Psi}_{1,t}$, Path 1 has higher complexity of $\mathcal{O}(N^3 P)$ due to the computation of the commutative term \mathbf{S}_t in the dense case. However, when matrices $\hat{\mathbf{W}}$ and $\hat{\Psi}_k$ are sparse in (18), Path 1 complexity can be reduced to $\mathcal{O}(S_{p,t}^2 P)$, where $S_{p,t}$ is as defined previously.

Algorithm 1 summarises our derived adaptive algorithm for learning $\hat{\mathbf{W}}_t$. Path 1 ignores Step 9 by setting $\mathbf{Q}_t = \mathbf{0}$, executing only Step 18 to account for shift-invariance. Conversely, Path 2 includes Step 9 but skips Steps 18-22, directly assigning $\hat{\mathbf{W}}_t = \hat{\Psi}_{1,t}$ instead. These two paths will be tested experimentally in subsequent sections.

C. Estimating \mathbf{h}_t

To fully identify the CGP model in (5), the graph filter coefficients $\hat{\mathbf{h}}_t$ remain to be estimated. This phase is optional since the primary objective of this work is to estimate the GSO structure. Notice that, $\hat{\mathbf{W}}_t$ must be *debiased* before estimating $\hat{\mathbf{h}}_t$, due to the heavy regularisation involved. Debiasing is performed by fixing and optimising only the non-zero elements of $\hat{\mathbf{W}}_t$ using least squares. Note that reducing the sample size in this way can risk distorting the noise distribution from normality, potentially compromising the minimum MSE criterion for noisy or small datasets [35].

After debiasing $\hat{\mathbf{W}}_t$, the filter coefficients $\hat{\mathbf{h}}_t$ are estimated. Unlike zeros in the GSO, which indicate absence of edges and thus have causal significance, sparsity in $\hat{\mathbf{h}}$ serves mainly to simplify the model structure. Given the more relaxed sparsity

Algorithm 1: Identifying the topology of $\hat{\mathbf{W}}$ ($\hat{\mathbf{W}}^*$)

Input : \mathbf{x}, P
Output: $\hat{\Psi}, \hat{\mathbf{W}}^*$

- 1 Initialise $\hat{\Psi}_0 = \hat{\Psi}_{+0} = \hat{\Psi}_{-0} = \mathbf{P}_0 = \mathbf{Q}_1 = \mathbf{0}$,
 $\hat{\mathbf{W}}_0 = \hat{\mathbf{W}}_{+0} = \hat{\mathbf{W}}_{-0} = \mathbf{S}_1 = \mathbf{0}$ and $\mathbf{R}_0 = \mathbf{0}$;
- 2 $t = 0$;
- 3 **do**
- 4 $t = t + 1$;
- 5 *Solving for $\hat{\Psi}_t$;*
- 6 $\mathbf{x}_{P,t} = [\mathbf{x}_{t-1}^T, \mathbf{x}_{t-2}^T, \dots, \mathbf{x}_{t-P}^T]^T$;
- 7 $\mathbf{R}_t = \lambda \mathbf{R}_{t-1} + \mathbf{x}_{P,t} \mathbf{x}_{P,t}^T$;
- 8 $\mathbf{P}_t = \lambda \mathbf{P}_{t-1} + \mathbf{x}_t \mathbf{x}_{P,t}^T$;
- 9 $\mathbf{Q}_t = [\mathbf{Q}_{1,t}, \mathbf{Q}_{2,t}, \dots, \mathbf{Q}_{P,t}]$ with $\mathbf{Q}_{p,t}$ according to (15);
- 10 calculate μ_t ;
- 11 $\mathbf{M}_t = [\mu_{1,t} \mathbf{1}_{N \times N}, \mu_{2,t} \mathbf{1}_{N \times N}, \dots, \mu_{P,t} \mathbf{1}_{N \times N}]$;
- 12 $\mathbf{G}_t = \hat{\Psi}_{t-1} \mathbf{R}_t - (\mathbf{P}_t - \gamma \mathbf{Q}_t)$;
- 13 calculate \mathbf{A}_t ;
- 14 $\hat{\Psi}_{+t} = \left(\hat{\Psi}_{+t-1} - (\mathbf{M}_t + \mathbf{G}_t)(\mathbf{A}_t \otimes \mathbf{I}_{N \times N}) \right)_+$;
- 15 $\hat{\Psi}_{-t} = \left(\hat{\Psi}_{-t-1} - (\mathbf{M}_t - \mathbf{G}_t)(\mathbf{A}_t \otimes \mathbf{I}_{N \times N}) \right)_+$;
- 16 $\hat{\Psi}_t = \hat{\Psi}_{+t} - \hat{\Psi}_{-t}$;
- 17 *Estimating $\hat{\mathbf{W}}_t$;*
- 18 \mathbf{S}_t according to (18);
- 19 $\mathbf{V}_t = \hat{\mathbf{W}}_{t-1} - (\hat{\Psi}_{1,t} - \gamma \mathbf{S}_t)$;
- 20 $\hat{\mathbf{W}}_{+t} = \left(\hat{\mathbf{W}}_{+t-1} - \beta_t (\mu_{1,t} \mathbf{1}_{N \times N} + \mathbf{V}_t) \right)_+$;
- 21 $\hat{\mathbf{W}}_{-t} = \left(\hat{\mathbf{W}}_{-t-1} - \beta_t (\mu_{1,t} \mathbf{1}_{N \times N} - \mathbf{V}_t) \right)_+$;
- 22 $\hat{\mathbf{W}}_t = \hat{\mathbf{W}}_{+t} - \hat{\mathbf{W}}_{-t}$;
- 23 **while** $t < T^*$ (an epoch with steady-state reached);
- 24 ; $\hat{\mathbf{W}}^* = \hat{\mathbf{W}}_{T^*}$.

requirements, GAR-LMS [33] is employed to arrive at the recursive update equation of $\hat{\mathbf{h}}$, given by

$$\hat{\mathbf{h}}_t = \hat{\mathbf{h}}_{t-1} + \rho_t \left(\mathbf{C}_t \hat{\mathbf{h}}_{t-1} - \mathbf{u}_t + \eta_t \mathbf{b}_t \right), \quad (19)$$

where

$$\mathbf{C}_t = \lambda \mathbf{C}_{t-1} + \mathbf{Y}_t^T \mathbf{Y}_t,$$

$$\mathbf{u}_t = \lambda \mathbf{u}_{t-1} + \mathbf{Y}_t^T \mathbf{x}_t,$$

$$\mathbf{b}_t : b_{i,t} = \frac{\text{sign}(\hat{h}_{i,t-1})}{\epsilon + \hat{h}_{i,t-1}},$$

where \mathbf{Y}_t contains the lagged graph shifted signals as in (11), $\mathbf{C}_t \in \mathbb{R}^{M \times M}$ tracks correlations between the shifted signals, $\mathbf{u}_t \in \mathbb{R}^M$ accumulates cross-correlations with the desired response, \mathbf{b}_t is the sparsity-promoting re-weighting vector, ρ_t is the stepsize, and ϵ prevents division by zero. This step could be further simplified by only taking the instantaneous samples into (19), that is, $\lambda = 0$, to yield

$$\hat{\mathbf{h}}_t = \hat{\mathbf{h}}_{t-1} + \rho_t \left(\mathbf{Y}_t^T \mathbf{e}_t + \eta_t \mathbf{b}_t \right)$$

where

$$\mathbf{e}_t = \mathbf{x}_t - \mathbf{Y}_t \hat{\mathbf{h}}_{t-1}.$$

Algorithm 2 summarises our derived adaptive algorithm for debiasing $\hat{\mathbf{W}}_t$ and estimating $\hat{\mathbf{h}}_t$. The cost of the debiasing phase is dominated by the term $\hat{\Psi}_{t-1} \mathbf{R}_t$, which has complexity

$\mathcal{O}(N^3P^2)$ in the dense case or $\mathcal{O}(S_{t-1}NP)$ with sparse operations. The cost of updating $\hat{\mathbf{h}}_t$ is dominated by computing $\mathbf{Y}_t^T \mathbf{Y}_t$, requiring $\mathcal{O}(NP^4)$ operations for $\mathbf{Y}_t \in \mathbb{R}^{N \times M}$ with $M = P(P+3)/2$. While appearing formidable, P is typically much smaller than N , so this update is unlikely to be the computational bottleneck in the overall algorithm.

Algorithm 2: Determining the *unbiased* $\hat{\mathbf{W}}$ and $\hat{\mathbf{h}}$

Input : \mathbf{x}, P, δ
Output: $\hat{\mathbf{W}}, \hat{\mathbf{h}}$

- 1 All recursive variables resume from Algorithm 1;
- 2 $t = T^*$;
- 3 **do**
- 4 $t = t + 1$;
- 5 *Debiasing* $\hat{\mathbf{W}}_t$;
- 6 $\mathbf{R}_t = \lambda \mathbf{R}_{t-1} + \mathbf{x}_{P,t} \mathbf{x}_{P,t}^T$;
- 7 $\mathbf{P}_t = \lambda \mathbf{P}_{t-1} + \mathbf{x}_t \mathbf{x}_t^T$;
- 8 $\mathbf{G}_t = \left(\hat{\Psi}_{t-1} \mathbf{R}_t - \mathbf{P}_t \right)_{\hat{\mathbf{W}}}$ where $(\cdot)_{\hat{\mathbf{W}}}$ is the projection to non-zero elements of $\hat{\Psi}$ considering $\hat{\mathbf{W}}$;
- 9 calculate \mathbf{A}_t ;
- 10 $\hat{\Psi}_t = \hat{\Psi}_{t-1} - \mathbf{G}_t (\mathbf{A}_t \otimes \mathbf{I}_{N \times N})$;
- 11 Setting $\hat{\mathbf{W}}_t = \hat{\Psi}_{1,t}$;
- 12 *Estimating* $\hat{\mathbf{h}}$;
- 13 $\mathbf{Y}_t = \left[\mathbf{x}_{t-1}, \hat{\mathbf{W}}_t \mathbf{x}_{t-1}, \dots, \mathbf{x}_{t-P}, \dots, \hat{\mathbf{W}}_t^P \mathbf{x}_{t-P} \right]$;
- 14 $\mathbf{e}_t = \mathbf{x}_t - \mathbf{Y}_t \hat{\mathbf{h}}_{t-1}$;
- 15 $\mathbf{b}_t : b_{i,t} = \frac{\text{sign}(\hat{h}_{i,t})}{\sigma + \hat{h}_{i,t}}$;
- 16 $\hat{\mathbf{h}}_t = \hat{\mathbf{h}}_{t-1} + \rho_t (\mathbf{Y}_t^T \mathbf{e}_t + \eta_t \mathbf{b}_t)$;
- 17 **while** $t < T$ (a terminal epoch);
- 18 $\hat{\mathbf{W}} = \hat{\mathbf{W}}_T, \hat{\mathbf{h}} = \hat{\mathbf{h}}_T$

D. Tuning Hyperparameters

Our algorithm requires tuning several hyperparameters: regularisation constants $\boldsymbol{\mu}_t := [\mu_{1,t}, \mu_{2,t}, \dots, \mu_{P,t}]^T$, η_t , γ and ϵ ; stepsizes \mathbf{A}_t , β_t and ρ_t ; and the forgetting factor λ .

Prior knowledge can guide many of these selections. For example, the ℓ_1 -norm related constants, following [36], we set

$$\mu_{p,t} = \mu_p \|\mathbf{P}_{p,t} - \gamma \mathbf{Q}_{p,t}\|_\infty,$$

$$\eta_t = \eta \|\mathbf{Y}_t^T \mathbf{x}_t\|_\infty,$$

where $\mathbf{P}_{p,t}$ is the p -th block of \mathbf{P}_t . Step sizes can be determined using Armijo line search [37] or adaptive signal processing theory for stable convergence. The entries of $\boldsymbol{\mu}$ could decrease with p to reflect the decreasing sparsity of higher-order graph filters in (1). The forgetting factor λ should be close to 1 to balance adaptability and stability. However, parameters η and γ are rather unconstrained and require empirical tuning.

E. A Note on Convergence

A rigorous convergence analysis for CGP identification is presented in [19]. However, the assumptions for successful convergence are quite restrictive, requiring both specific sparsity structures (Assumption A5 in [19]) and strong stability conditions (Assumptions A4 and A6 in [19]). Attempts to

relax these assumptions have had limited success, partly due to inherent biases in the base problem (8). For instance, the ℓ_1 -norm regularisation tends to underestimate non-zero elements [36], and the commutator term adds further complexity.

Given these theoretical limitations, we complement our analysis with empirical convergence metrics. Specifically, we evaluate precision, recall, and F1 scores for identifying non-zero elements in \mathbf{W} , independent of their exact values.

V. EXPERIMENTS ON SYNTHETIC DATA

To assess the performance and convergence characteristics of our algorithm variants across different graph topologies, the Normalised Mean Square Error (NMSE) was utilised as the primary metric to assess the convergence of three key aspects of our model: the prediction error from the estimated graph filter,

$$\text{NMSE}(\mathbf{x}_\Psi) = \frac{\|\mathbf{x}_t - \hat{\Psi}_{t-1} \mathbf{x}_{P,t}\|_2^2}{\|\mathbf{x}_t\|_2^2}, \quad (20)$$

the prediction error from the estimated graph filter coefficients,

$$\text{NMSE}(\mathbf{x}_h) = \frac{\|\mathbf{x}_t - \mathbf{Y}_t \hat{\mathbf{h}}_{t-1}\|_2^2}{\|\mathbf{x}_t\|_2^2}, \quad (21)$$

and the error in the estimated GSO matrix,

$$\text{NMSE}(\mathbf{W}) = \frac{\|\mathbf{W} - \hat{\mathbf{W}}_t\|_F^2}{\|\mathbf{W}\|_F^2}, \quad (22)$$

where $(\hat{\cdot})$ denotes the estimated parameters and $\|\cdot\|_F$ is the Frobenius norm. Additionally, we evaluate convergence through precision, recall, and F1 scores for the classification of non-zero elements in \mathbf{W} , and report the missing rate (P_M) and false alarm rate (P_{FA}) of edges once the model is in steady-state.

A. Data Generation

The AdaCGP algorithm was evaluated across four graph topologies: random (R), Erdős-Rényi (ER) [38], K-Regular (KR), and Stochastic Block Model (SBM) [39], each with $N = 50$ nodes. The random graph weights were drawn from $\mathcal{N}(0, 1)$, thresholded between $0.3w_{\max}$ and $0.7w_{\max}$ (w_{\max} being the maximum absolute weight), and normalised by 1.5 times the largest eigenvalue. For the ER graph, edges from $\mathcal{N}(0, 1)$ were thresholded between 1.6 and 1.8 in absolute value ($p_{ER} \approx 0.04$), soft thresholded by 1.5 to range between 0.1 and 0.3, and normalised by 1.5 times the largest eigenvalue. The KR graph assigned 3 nearest-neighbor connections per node with weights from $\mathcal{U}(0.5, 1.0)$, normalised by 1.1 times the largest eigenvalue. The SBM graph comprised $k = 10$ equal-sized clusters, with intra-cluster connection probability 0.05 and inter-cluster probabilities uniform in $[0, 0.04]$. Edge weights were sampled from a Laplacian distribution with rate $\lambda_e = 2$, normalised by 1.1 times the largest eigenvalue.

Following [19], we set model order to $P = 3$ and generated sparse filter coefficients h_{ij} ($2 \leq i \leq P$, $0 \leq j \leq i$) from $2^{i+j} h_{ij} \sim 0.5\mathcal{U}(-1, -0.45) + 0.5\mathcal{U}(0.45, 1)$, normalised by 1.5 for stability. Graph signals, $\mathbf{x}_t \in \mathbb{R}^{N \times 1}$, were then generated recursively from (5) with $\mathbf{x}_{t \leq P} = \mathbf{0}$ and $\mathbf{w}_t \sim \mathcal{N}(\mathbf{0}, \mathbf{I}_N)$.

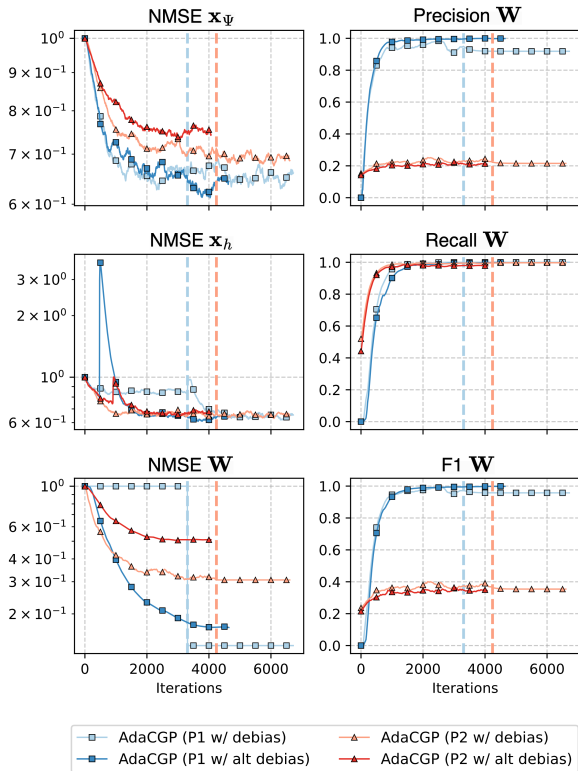


Fig. 1. Convergence of AdaCGP variants on the K-Regular topology in NMSE (\mathbf{x}_Ψ , \mathbf{x}_h , \mathbf{W}) and the metrics for classification of non-zero elements in \mathbf{W} (Precision, Recall, F1). Vertical dashed lines indicate debiasing onset.

From 10,500 generated samples, we discarded the first 500 to account for transitory effects and retained 10,000 for analysis. After hyperparameter optimisation, this process was repeated 20 times to construct Monte Carlo estimates of our metrics and parameters.

B. Estimators: AdaCGP Variants and Baseline Models

We evaluated four AdaCGP variants defined by two design choices: which implementation of Algorithm 1 (Path 1, P1, or Path 2, P2), and when to apply Algorithm 2 (after Algorithm 1 reaches steady-state or in alternation at each time step). These variants were: 1) AdaCGP (P1 w/ debias), 2) AdaCGP (P1 w/ alt debias), 3) AdaCGP (P2 w/ debias), and 4) AdaCGP (P2 w/ alt debias).

Steady-state detection was used to perform early stopping of Algorithms 1 and 2. It utilises exponential moving averages of the observable metrics NMSE(\mathbf{x}_Ψ) and NMSE(\mathbf{x}_h), denoted as $\sigma_t^{(1)}$ and $\sigma_t^{(2)}$ respectively, where $\sigma_t = \alpha\sigma_{t-1} + (1 - \alpha)\text{NMSE}_t$ with $\alpha = 0.995$. Steady-state is reached when the moving average fails to improve by 1% within 250 epochs. For Algorithm 1, we monitored $\sigma_t^{(1)}$ convergence to control the switch to Algorithm 2, as at this stage $\hat{\mathbf{h}}$ may not be meaningful due to bias in $\hat{\mathbf{W}}$. For Algorithm 2, $\sigma_t^{(2)}$ convergence determines early stopping and defines the terminal epoch. For alternating debiasing, only $\sigma_t^{(2)}$ is monitored.

Hyperparameter optimisation for each variant used a random grid search over 10,000 trials, sampling elements of $\boldsymbol{\mu}$

TABLE I
PERFORMANCE COMPARISON OF ADACGP VARIANTS AND BASELINE MODELS (TIRSO, TISO) IN STEADY-STATE FOR THE K-REGULAR TOPOLOGY. VALUES SHOW MEDIAN \pm INTERQUARTILE RANGE ACROSS TRIALS. BEST RESULTS ARE SHOWN IN BOLD, AND SECOND-BEST ARE UNDERLINED.

Method	NMSE(\mathbf{W})	P_M	P_{FA}
TIRSO	0.79 \pm 0.02	0.00 \pm 0.00	1.00 \pm 0.00
TISO	0.78 \pm 0.02	0.00 \pm 0.00	1.00 \pm 0.00
P2 w/ alt. debias	0.51 \pm 0.02	0.02 \pm 0.01	0.61 \pm 0.03
P2 w/ debias	0.33 \pm 0.02	0.01 \pm 0.00	0.53 \pm 0.10
P1 w/ alt. debias	0.21 \pm 0.04	0.01 \pm 0.01	0.00 \pm 0.00
P1 w/ debias	0.14 \pm 0.02	0.00 \pm 0.00	<u>0.01 \pm 0.02</u>

uniformly from (0.001, 1], η from (0.005, 0.1] with step 0.005, γ from (0.05, 2.0] with step 0.05, and λ from (0.80-0.99] with step 0.01. The best parameters were selected by minimising the average of NMSE(\mathbf{x}_h) during the final patience epochs of steady-state.

We benchmarked against TISO and TIRSO [24], sparse adaptive VAR models that track time-varying causality graphs online using LMS and RLS approaches, respectively. Unlike our method, these baselines do not model structural dependencies between parameters, like shift-invariance. In these cases, graph topology estimates \mathbf{W}_t are derived from the notion of VAR causality [24], where element (i, j) is causal if $\sum_{p=1}^P \mathbb{1}(\Psi_{ij}^{(p)} \neq 0) > 0$, with weights assigned to causal edges as $\mathbf{W}_{ij} = \|\Psi_{ij}\|_2 \cdot \text{causal}_{ij}$. For TISO, the sparsity hyperparameters span (0.025, 1.0] with step 0.025, while TIRSO additionally samples forgetting factors from (0.80-0.99] with step 0.01, optimising for minimal steady-state prediction error NMSE(\mathbf{x}_Ψ).

To ensure optimal convergence, all models employed an adaptive step size α_t (with $\mathbf{A}_t = \alpha_t \mathbf{I}_P$), computed as

$$\alpha_t = \frac{2}{\lambda_{\max}(\mathbf{R}_t)} \cdot \frac{1}{\|\mathbf{x}_{P,t}\|_2^2 + \epsilon}, \quad (23)$$

where ϵ ensures numerical stability. Other stepsizes β_t and ρ_t were calculated using the Armijo rule for automatic selection.

C. Convergence Across Graph Topologies

Fig. 1 shows the convergence of our metrics for the KR topology as a representative example. All models converge to low non-zero values for NMSE(\mathbf{x}_Ψ) and NMSE(\mathbf{x}_h), with Path 1 achieving lower errors than Path 2. The NMSE(\mathbf{x}_h) for Path 1 showed significant improvement post-debiasing, and achieved near-zero NMSE(\mathbf{W}). While alternating debiasing converged to slightly higher values than steady-state debiasing, it demonstrated faster convergence in NMSE(\mathbf{W}) for Path 1.

The considered methods exhibited distinct differences in Precision(\mathbf{W}), with Path 1 maintaining near-perfect precision (≈ 1.0) compared to Path 2's plateau around 0.2. All variants achieved high Recall(\mathbf{W}) (≈ 1.0), though Path 2 showed faster initial increases. The F1 scores strongly favour Path 1 (≈ 1.0 versus ≈ 0.4), with the alternating debiasing variant showing marginally better precision due to its iteration-by-iteration

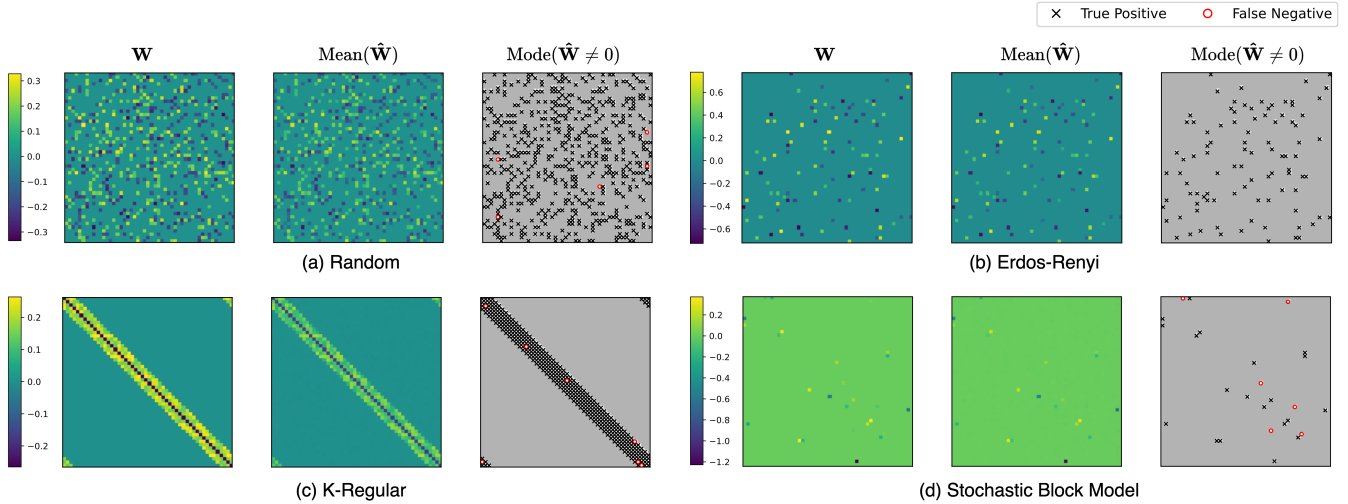


Fig. 2. GSO matrices across four graph topologies: (a) Random, (b) Erdős-Rényi, (c) K-Regular, and (d) Stochastic Block Model. For each topology we show: true GSO \mathbf{W} (left), mean estimate $\text{Mean}(\hat{\mathbf{W}})$ over 20 realisations (middle), and most commonly estimated non-zero elements $\text{Mode}(\hat{\mathbf{W}} \neq 0)$ with highlighted true positives and false negatives (right). Results shown for the best-performing AdaCGP variant based on steady-state $\text{NMSE}(\mathbf{x}_h)$.

approach providing greater robustness to noise and misspecification of non-zero elements upon entering Algorithm 2.

As shown in Table I, the AdaCGP variants consistently outperformed the baselines. The AdaCGP (P1 w/ debias) achieves an 82% reduction in $\text{NMSE}(\mathbf{W})$ compared to TISO (0.14 ± 0.02 versus 0.78 ± 0.02) and a 58% reduction compared to P2 w/ debias (0.33 ± 0.02). Notably, Path 1 variants maintained near-zero false alarm rates ($P_{FA} \leq 0.01$) while achieving minimal missing edge rates ($P_M \leq 0.01$), in contrast to baseline models' P_{FA} of 1.00 and Path 2's P_{FA} exceeding 0.50. The baseline models' P_{FA} of 1.00 reflected their sparsity mechanisms' inability to explicitly set elements to zero, while our variable splitting approach overcame this limitation, effectively identifying and removing irrelevant edges for an improved P_{FA} and P_M trade-off.

D. Identification of the GSO Topology

Fig. 2 compares the true and estimated GSO matrices across the R, ER, KR, and SBM topologies. For each topology, we show the true GSO \mathbf{W} alongside the mean estimate over 20 realisations, $\text{Mean}(\hat{\mathbf{W}})$, from the best-performing AdaCGP variant (based on lowest steady-state $\text{NMSE}(\mathbf{x}_h)$). While there is some bias in the estimated element values, particularly in the KR topology, the relative edge weights and overall structure were well preserved.

A comparison of the most common non-zero elements over realisations, $\text{Mode}(\hat{\mathbf{W}} \neq 0)$, to the true elements in \mathbf{W} reveals no false positives as the most frequent outcome, with minimal false negatives. This demonstrates the effectiveness of AdaCGP's sparse algorithm in explicitly zeroing out GSO matrix elements while identifying most of the true edges.

E. The Effect of Sparsity Regularisation on Performance

To investigate how estimated network sparsity relates to $\text{NMSE}(\mathbf{x}_h)$, a practical metric for hyperparameter tuning that does not require knowledge of the true network structure, we

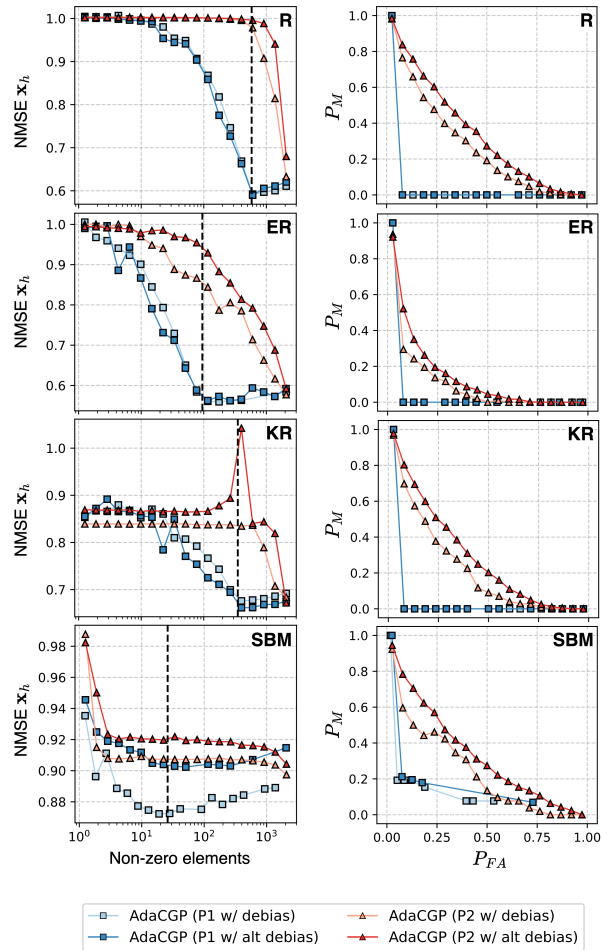


Fig. 3. Performance of the AdaCGP variants for different graph topologies: R, ER, KR and SBM. Left column: $\text{NMSE}(\mathbf{x}_h)$ vs. estimated non-zeros in $\hat{\mathbf{W}}$. Vertical dashed lines indicate the true number of non-zeros. Right column: Probability of missing edges (P_M) vs. probability of false alarm (P_{FA}).

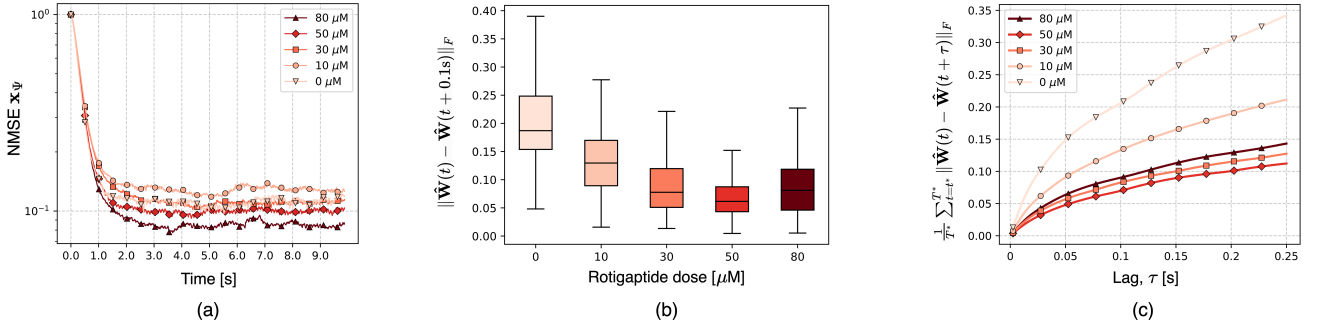


Fig. 4. Global analysis of fibrillation dynamics across varying rotigaptide concentrations. (a) Prediction error $\text{NMSE}(\mathbf{x}_\Psi)$ over time, showing lower steady-state errors with increasing concentrations. (b) Distribution of Frobenius norms between $\mathbf{W}(t)$ and $\mathbf{W}(t + 0.1s)$ in steady-state, indicating more stable dynamics at higher concentrations. (c) Mean Frobenius norm as a function of time lag, demonstrating more gradual changes in graph structure for higher concentrations.

experimented with varying the sparsity regularisation strength. Using the best-performing hyperparameters from the AdaCGP variants from before, we randomly sampled elements of μ uniformly from $(0.001, 1]$ across 5,000 trials per model variant and different graph types with $N = 50$ nodes.

Fig. 3 shows the $\text{NMSE}(\mathbf{x}_h)$ versus non-zero elements in \mathbf{W} (left column) and P_M versus P_{FA} trade-offs (right column), where the x-axis has been uniformly binned and median results displayed. As expected, increasing sparsity regularisation reduces the estimated number of non-zero elements and increases P_M . Path 1 variants minimised $\text{NMSE}(\mathbf{x}_h)$ near the true sparsity level, while Path 2 variants overestimated the number of non-zero elements. Path 1 consistently achieved lower $\text{NMSE}(\mathbf{x}_h)$ and superior P_M - P_{FA} trade-offs across all topologies, exhibiting near-perfect performance with very low P_M and P_{FA} . These results demonstrate that optimising $\text{NMSE}(\mathbf{x}_h)$ for Path 1 variants leads to accurate network sparsity estimation and thus improved causal discovery.

VI. ASSESSING THE STRUCTURE AND STABILITY OF CARDIAC FIBRILLATION

While existing applications of Granger causality to fibrillation dynamics [40] use batch processing to capture average propagation patterns, our online algorithm tracks temporal changes in GSO weights and causal structure. This enables assessment of propagation patterns and their stability at both global and local levels, having the potential to inform clinical evaluations of the electrophenotype, where propagation appears chaotic yet maintains quantifiable structure [41]–[43]. Such dynamic assessment could identify the stable conduction patterns maintaining arrhythmias, directly supporting diagnosis and treatment strategies.

To demonstrate these capabilities, we analysed optical mapping data of VF from an ex vivo Sprague-Dawley (SD, Charles River, Harlow, UK) rat heart during sequential administration of rotigaptide at concentrations in micromolar (μM), an anti-arrhythmic drug shown to induce more organised dynamics [43]. All procedures were performed in accordance with the UK Animals (Scientific Procedures) Act 1986 and ARRIVE guidelines, and were approved by the Imperial College London Ethical Review Board (project licences PEE7C76CD and PCA5EE967). Animal procedures conformed to guidelines

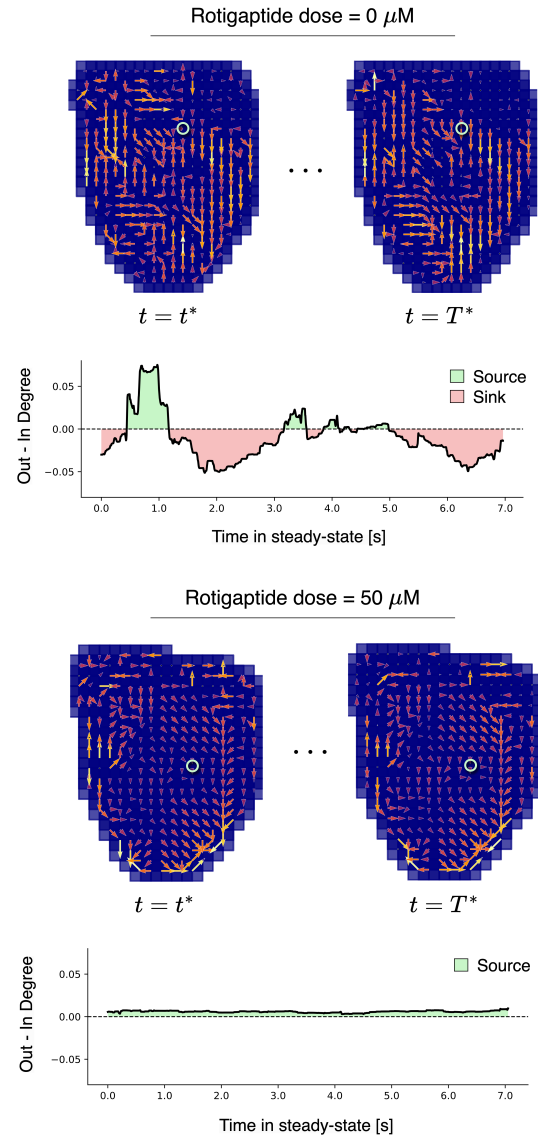


Fig. 5. Local stability analysis of fibrillation dynamics. Net edge directions at steady-state start ($t = t^*$) and end ($t = T^*$) for VF ($0 \mu\text{M}$, top) and rotigaptide $50 \mu\text{M}$ (bottom). Colour and arrow length denote edge weights. Time series show Out-In Degree for circled region during steady-state, demonstrating alternating source-sink behaviour in VF versus stable source characteristics at $50 \mu\text{M}$.

from Directive 2010/63/EU of the European Parliament on the protection of animals used for scientific purposes. Rats were anaesthetised with 5% isoflurane (95% oxygen mix) and euthanised via cervical dislocation prior to heart explantation.

The experiment records fluorescence signals proportional to cardiac action potential using a 128×80 pixel camera at 1000 Hz. Recordings span 10s during administration of rotigaptide in concentrations of 0, 10, 30, 50, and 80 μM , where zero represents baseline VF. After following the preprocessing steps in [43], we downsampled the spatial resolution by a factor 4 to ≈ 350 nodes and extracted Hilbert phase angles as graph signals \mathbf{x}_t , which capture each region's position in its oscillatory cycle.

AdaCGP (P1 w/ alt debias) is deployed with gradients constrained to adjacent pixels to reflect the local connectivity of cardiac tissue. The model uses parameters $P = 3$, $\gamma = 1$, $\eta = 0.01$, elements of $\boldsymbol{\mu}$ as 0.1, and $\lambda = 0.5$, with low forgetting factor enabling rapid adaptation. Stepsizes were calculated using the Armijo rule for automatic selection.

Fig. 4 reveals three aspects of global stability. First, NMSE(\mathbf{x}_ψ) showed lower steady-state errors with increasing rotigaptide concentrations, suggesting more organised and predictable dynamics consistent with the drug's anti-arrhythmic nature [44]. Second, Frobenius norms between successive GSOs ($\hat{\mathbf{W}}(t)$ and $\hat{\mathbf{W}}(t+0.1\text{s})$) exhibited lower median values and less variability at higher concentrations, indicating more stable global dynamics. Finally, mean Frobenius norm error increased more gradually with time lag at higher concentrations compared to VF (0 μM) and low concentrations, further supporting enhanced global stability with increased rotigaptide concentration.

Fig. 5 demonstrates local stability through edge patterns at the start (t^*) and end (T^*) of steady-state. During VF (0 μM), the magnitude and direction of net edges varied considerably between t^* and T^* , indicating unstable propagation patterns. The highlighted region's Out-In Degree ($\sum_j \hat{W}_{ij} - \sum_i \hat{W}_{ij}$) fluctuated significantly between positive (source) and negative (sink) values, further demonstrating this instability. In contrast, at 50 μM , edge magnitudes and directions across time points remained largely consistent, suggesting more stable propagation patterns. This stability is quantified by the highlighted region's behaviour, which maintains consistent source characteristics with minimal Out-In Degree variations that are significantly lower than during VF.

VII. CONCLUSION

We have developed AdaCGP, an online time-vertex adaptive filtering algorithm for tracking time-varying causal graph structures in multivariate time series. Our approach introduced a variable splitting approach for sparse adaptive filtering to efficiently identify the GSO in real-time and reliably estimate its causal elements from streaming data. Experiments across various graph topologies have demonstrated AdaCGP's superior performance over existing adaptive VAR models in both prediction accuracy and graph structure recovery. Path 1 variants have showed particularly strong performance in causal discovery while maintaining low false positive rates,

with prediction error minimisation proving effective for hyperparameter tuning and accurate sparsity estimation. Application to rat VF data revealed AdaCGP's potential for analysing complex cardiac arrhythmia. The algorithm has successfully tracked changes in cardiac organisation under varying rotigaptide concentrations, providing insights into the structure and stability of fibrillation at both global and local levels. Upon further trials in humans, this approach could help identify critical mechanisms sustaining the disorder, paving the way for personalised treatment strategies and potentially improved outcomes. Future developments could extend our framework to non-linear adaptive filtering and incorporate domain-specific GSO constraints through our variable splitting approach. Such extensions could improve the modelling of non-linear dynamical systems, such as cardiac fibrillation, where non-linear filters could better capture the chaotic dynamics and constrained GSOs, like the anisotropic Laplacian or energy-preserving shift operators [45], would more closely align with established physical models of cardiac conduction [46]. Overall, this work provides a principled and efficient framework for tracking evolving causal relationships in streaming data, bridging the gap between GSP theory and adaptive signal processing for real-time graph structure learning.

ACKNOWLEDGMENTS

Alexander Jenkins is supported by the UKRI CDT in AI for Healthcare <http://ai4health.io> (Grant No. P/S023283/1). Fu Siong Ng is supported by the British Heart Foundation (RG/F/22/110078, FS/CRTF/21/24183 and RE/19/4/34215) and the National Institute for Health Research Imperial Biomedical Research Centre.

REFERENCES

- [1] T. Varidhisai and D. Mandic, "Methods of adaptive signal processing on graphs using vertex-time autoregressive models," *arXiv preprint arXiv:2003.05729*, 2020.
- [2] W. Y. Yi, K. M. Lo, T. Mak, K. S. Leung, Y. Leung, and M. L. Meng, "A survey of wireless sensor network based air pollution monitoring systems," *Sensors*, vol. 15, no. 12, pp. 31392–31427, 2015.
- [3] V. C. Gungor, B. Lu, and G. P. Hancke, "Opportunities and challenges of wireless sensor networks in smart grid," *IEEE Transactions on Industrial Electronics*, vol. 57, no. 10, pp. 3557–3564, 2010.
- [4] Y. Rudy, "Noninvasive ECG imaging (ECGI): Mapping the arrhythmic substrate of the human heart," *International Journal of Cardiology*, vol. 237, pp. 13–14, 2017.
- [5] A. Sau, S. Al-Aidarous, J. Howard, J. Shalhoub, A. Sohaib, M. Shun-Shin, P. G. Novak, R. Leather, L. D. Sterns, C. Lane *et al.*, "Optimum lesion set and predictors of outcome in persistent atrial fibrillation ablation: a meta-regression analysis," *EP Europace*, vol. 21, no. 8, pp. 1176–1184, 2019.
- [6] F. S. Ng, B. S. Handa, X. Li, and N. S. Peters, "Toward mechanism-directed electrophenotype-based treatments for atrial fibrillation," *Frontiers in Physiology*, vol. 11, p. 987, 2020.
- [7] D. Scherr, P. Khairy, S. Miyazaki, V. Aurillac-Lavignolle, P. Pascale, S. B. Wilton, K. Ramoul, Y. Komatsu, L. Roten, A. Jadidi *et al.*, "Five-year outcome of catheter ablation of persistent atrial fibrillation using termination of atrial fibrillation as a procedural endpoint," *Circulation: Arrhythmia and Electrophysiology*, vol. 8, no. 1, pp. 18–24, 2015.
- [8] L. Stanković, D. Mandic, M. Daković, M. Brajović, B. Scalzo, S. Li, and A. G. Constantinides, "Data analytics on graphs. Part I: Graphs and spectra on graphs," *Foundations and Trends® in Machine Learning*, vol. 13, no. 1, pp. 1–157, 2020.
- [9] L. Stanković, D. Mandic, M. Daković, M. Brajović, B. Scalzo, S. Li, and A. G. Constantinides, "Data analytics on graphs. Part II: Signals on graphs," *Foundations and Trends® in Machine Learning*, vol. 13, no. 2-3, pp. 158–331, 2020.

- [10] L. Stanković, D. Mandić, M. Daković, M. Brajović, B. Scalzo, S. Li, and A. G. Constantinides, "Data analytics on graphs. Part III: Machine learning on graphs, from graph topology to applications," *Foundations and Trends® in Machine Learning*, vol. 13, no. 4, pp. 332–530, 2020.
- [11] J. Friedman, T. Hastie, and R. Tibshirani, "Sparse inverse covariance estimation with the graphical lasso," *Biostatistics*, vol. 9, no. 3, pp. 432–441, 12 2007.
- [12] V. Kalofolias, "How to learn a graph from smooth signals," in *Proceedings of the 19th International Conference on Artificial Intelligence and Statistics (AISTATS)*, vol. 51. Cadiz, Spain: PMLR, 2016, pp. 920–929.
- [13] X. Dong, D. Thanou, P. Frossard, and P. Vandergheynst, "Learning Laplacian matrix in smooth graph signal representations," *IEEE Transactions on Signal Processing*, vol. 64, no. 23, pp. 6160–6173, 2016.
- [14] B. Pasdoloup, V. Gripon, G. Mercier, D. Pastor, and M. G. Rabbat, "Characterization and inference of graph diffusion processes from observations of stationary signals," *IEEE Transactions on Signal and Information Processing over Networks*, vol. 4, no. 3, pp. 481–496, 2018.
- [15] D. Thanou, X. Dong, D. Kressner, and P. Frossard, "Learning heat diffusion graphs," *IEEE Transactions on Signal and Information Processing over Networks*, vol. 3, no. 3, pp. 484–499, 2017.
- [16] S. Segarra, A. G. Marques, G. Mateos, and A. Ribeiro, "Network topology inference from spectral templates," *IEEE Transactions on Signal and Information Processing over Networks*, vol. 3, no. 3, pp. 467–483, 2017.
- [17] C. W. Granger, "Investigating causal relations by econometric models and cross-spectral methods," *Econometrica: Journal of the Econometric Society*, pp. 424–438, 1969.
- [18] S. Segarra, G. Mateos, A. G. Marques, and A. Ribeiro, "Blind identification of graph filters," *IEEE Transactions on Signal Processing*, vol. 65, no. 5, pp. 1146–1159, 2017.
- [19] J. Mei and J. M. Moura, "Signal processing on graphs: Causal modeling of unstructured data," *IEEE Transactions on Signal Processing*, vol. 65, no. 8, pp. 2077–2092, 2016.
- [20] W. Q. Arnaud Casteigts, Paola Flocchini and N. Santoro, "Time-varying graphs and dynamic networks," *International Journal of Parallel, Emergent and Distributed Systems*, vol. 27, no. 5, pp. 387–408, 2012.
- [21] B. Widrow and M. E. Hoff, *Adaptive switching circuits*. Cambridge, MA, USA: MIT Press, 1988, p. 123–134.
- [22] A. H. Sayed, *Fundamentals of adaptive filtering*. John Wiley & Sons, 2003.
- [23] T. Varidhdhisai and D. P. Mandić, "On an RLS-like LMS adaptive filter," in *Proceedings of the 22nd International Conference on Digital Signal Processing (DSP)*, 2017, pp. 1–5.
- [24] B. Zaman, L. M. L. Ramos, D. Romero, and B. Beferull-Lozano, "Online topology identification from vector autoregressive time series," *IEEE Transactions on Signal Processing*, vol. 69, pp. 210–225, 2020.
- [25] P. Di Lorenzo, S. Barbarossa, P. Banelli, and S. Sardellitti, "Adaptive least mean squares estimation of graph signals," *IEEE Transactions on Signal and Information Processing over Networks*, vol. 2, no. 4, pp. 555–568, 2016.
- [26] Y. Yan, E. E. Kuruoglu, and M. A. Altinkaya, "Adaptive sign algorithm for graph signal processing," *Signal Processing*, vol. 200, p. 108662, 2022.
- [27] P. Di Lorenzo, P. Banelli, S. Barbarossa, and S. Sardellitti, "Distributed adaptive learning of graph signals," *IEEE Transactions on Signal Processing*, vol. 65, no. 16, pp. 4193–4208, 2017.
- [28] E. Isufi, A. Loukas, N. Perraudin, and G. Leus, "Forecasting time series with VARMA recursions on graphs," *IEEE Transactions on Signal Processing*, vol. 67, no. 18, pp. 4870–4885, 2019.
- [29] A. G. Marques, S. Segarra, G. Leus, and A. Ribeiro, "Stationary graph processes and spectral estimation," *IEEE Transactions on Signal Processing*, vol. 65, no. 22, pp. 5911–5926, 2017.
- [30] F. Edition, A. Papoulis, and S. U. Pillai, *Probability, random variables, and stochastic processes*. McGraw-Hill Europe: New York, NY, USA, 2002.
- [31] Y. Chen, Y. Gu, and A. O. Hero, "Sparse LMS for system identification," in *Proceedings of the IEEE International Conference on Acoustics, Speech and Signal Processing (ICASSP)*. IEEE, 2009, pp. 3125–3128.
- [32] R. C. de Lamare and R. Sampaio-Neto, "Sparsity-aware adaptive algorithms based on alternating optimization and shrinkage," *IEEE Signal Processing Letters*, vol. 21, no. 2, pp. 225–229, 2014.
- [33] O. Taheri and S. A. Vorobyov, "Sparse channel estimation with l_p -norm and reweighted l_1 -norm penalized least mean squares," in *Proceedings of the IEEE International Conference on Acoustics, Speech and Signal Processing (ICASSP)*, 2011, pp. 2864–2867.
- [34] M. Schmidt, G. Fung, and R. Rosales, "Fast optimization methods for L_1 regularization: A comparative study and two new approaches," in *Proceedings of the 18th European Conference on Machine Learning (ECML)*. Berlin, Heidelberg: Springer Berlin Heidelberg, 2007, pp. 286–297.
- [35] D. Donoho, "De-noising by soft-thresholding," *IEEE Transactions on Information Theory*, vol. 41, no. 3, pp. 613–627, 1995.
- [36] S.-J. Kim, K. Koh, M. Lustig, S. Boyd, D. Gorinevsky *et al.*, "A method for large-scale L_1 -regularized least squares," *IEEE Journal on Selected Topics in Signal Processing*, vol. 1, no. 4, pp. 606–617, 2007.
- [37] C. Boukis, D. P. Mandić, A. G. Constantinides, and L. Polymenakos, "A modified Armijo rule for the online selection of learning rate of the LMS algorithm," *Digital Signal Processing*, vol. 20, no. 3, pp. 630–639, 2010.
- [38] P. Erdos, A. Rényi *et al.*, "On the evolution of random graphs," *Publications of the Mathematical Institute of the Hungarian Academy of Sciences*, vol. 5, no. 1, pp. 17–60, 1960.
- [39] A.-L. Barabási and R. Albert, "Emergence of scaling in random networks," *Science*, vol. 286, no. 5439, pp. 509–512, 1999.
- [40] B. S. Handa, X. Li, K. K. Aras, N. A. Qureshi, I. Mann, R. A. Chowdhury, Z. I. Whinnett, N. W. Linton, P. B. Lim, P. Kanagaratnam *et al.*, "Granger causality-based analysis for classification of fibrillation mechanisms and localization of rotational drivers," *Circulation: Arrhythmia and Electrophysiology*, vol. 13, no. 3, p. e008237, 2020.
- [41] S. Petrutiu, J. Ng, G. M. Nijm, H. Al-Angari, S. Swiryn, and A. V. Sahakian, "Atrial fibrillation and waveform characterization," *IEEE Engineering in Medicine and Biology Magazine*, vol. 25, no. 6, pp. 24–30, 2006.
- [42] J. J. Sanchez-Munoz, J. L. Rojo-Alvarez, A. Garcia-Alberola, E. Everss, F. Alonso-Atienza, M. Ortiz, J. Martinez-Sanchez, J. Ramos-Lopez, and M. Valdes-Chavari, "Spectral analysis of intracardiac electrograms during induced and spontaneous ventricular fibrillation in humans," *Europace*, vol. 11, no. 3, pp. 328–331, 2009.
- [43] B. S. Handa, X. Li, N. Baxan, C. H. Roney, A. Shchendrygina, C. A. Mansfield, R. J. Jabbour, D. S. Pitcher, R. A. Chowdhury, N. S. Peters *et al.*, "Ventricular fibrillation mechanism and global fibrillatory organization are determined by gap junction coupling and fibrosis pattern," *Cardiovascular Research*, vol. 117, no. 4, pp. 1078–1090, 2021.
- [44] Y.-C. Hsieh, J.-C. Lin, C.-Y. Hung, C.-H. Li, S.-F. Lin, H.-I. Yeh, J.-L. Huang, C.-P. Lo, K. Haugan, B. D. Larsen *et al.*, "Gap junction modifier rotigaptide decreases the susceptibility to ventricular arrhythmia by enhancing conduction velocity and suppressing discordant alternans during therapeutic hypothermia in isolated rabbit hearts," *Heart Rhythm*, vol. 13, no. 1, pp. 251–261, 2016.
- [45] B. Scalzo, L. Stanković, M. Daković, A. G. Constantinides, and D. P. Mandić, "A class of doubly stochastic shift operators for random graph signals and their boundedness," *Neural Networks*, vol. 158, pp. 83–88, 2023.
- [46] F. Fenton and A. Karma, "Vortex dynamics in three-dimensional continuous myocardium with fiber rotation: Filament instability and fibrillation," *Chaos: An Interdisciplinary Journal of Nonlinear Science*, vol. 8, no. 1, pp. 20–47, 03 1998.